

Resistive Switching in Tantalum Oxide with Varying Oxygen Content

Adam Zachary Blonsky

Physics, University of Wisconsin - Madison

NNIN iREU Site: Institut Für Bio- Und Nanosysteme (IBN), Forschungszentrum, Jülich, Germany

NNIN iREU Principal Investigator: Dr. Regina Dittmann, PGI-7, Jülich Forschungszentrum

NNIN iREU Mentor: Katharina Skaja, PGI-7, Jülich Forschungszentrum

Contact: azblonsky@gmail.com r.dittmann@fz-juelich.de k.skaja@fz-juelich.de

Abstract:

Silicon based non-volatile memory is nearing its practical limit and several other possibilities are being examined more closely as potential replacements. One of these possible replacements is resistive switching. Resistive switching is a phenomenon in which a metal-insulator-metal (MIM) structure can change to a low resistance state (LRS) at the application of a set voltage and then be switched back to a high resistance state (HRS) by the application of a reset voltage [1]. Much about resistive switching is still unknown in regards to which materials switch and why. Our group examined how the various set and reset voltages of tantalum oxide (TaO_x) changed when prepared with different oxygen to argon ratios during sputtering. By performing electrical characterization of the samples with a basic probe station, we were able to determine the set and reset voltages of each sample, each with differing oxygen contents during formation. Ultimately it was found that the oxygen content during sample preparation changed the initial resistance as expected but did not change the set or reset voltages.

Introduction:

Resistive switching is an interesting phenomenon of certain metal-insulator-metal (MIM) devices where, when a threshold

voltage, called the forming voltage, is applied to them, the resistance changes by orders of magnitude. This switching may then be undone by the application of another voltage, called the reset voltage, in the opposite direction, or it may be redone by applying a slightly lower threshold voltage in the original direction and is called the set voltage. This set-reset action can then be cycled. It is thought that the mechanism behind resistive switching is filamentary switching in which a controlled breakdown of the MIM device, caused by the forming voltage, allows for the creation of a conductive filament through the insulator [2]. This filament is then partially destroyed when the reset voltage is applied and is repaired when the set voltage is applied as shown in Figure 1.

Methodology:

In this project, we examined TaO_x , which is a very stable resistive switching material [2]. More specifically we aimed to discover how the switching characteristics of TaO_x (forming, set, and reset voltages) changed when the ratio of argon to oxygen was changed during the initial preparation of the samples. This oxygen to argon ratio was manipulated during the reactive sputtering of the TaO_x and was done in steps of 5% oxygen

starting from 10% oxygen to argon all the way to 25% oxygen to argon. The full process of sputtering and device fabrication is outlined in Figure 2.

After the devices were fabricated, characterization was done with an automatic IV probe station. The probe station characterized the $1.5 \mu\text{m}$ pad size probe and

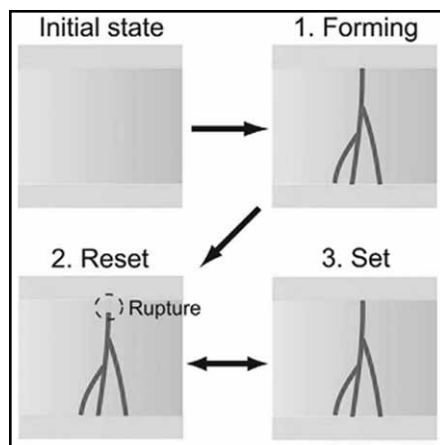


Figure 1: Simple model of the filamentary mechanism [3]. A conductive path is created that provides a low resistance path and then is reset to the original resistance.

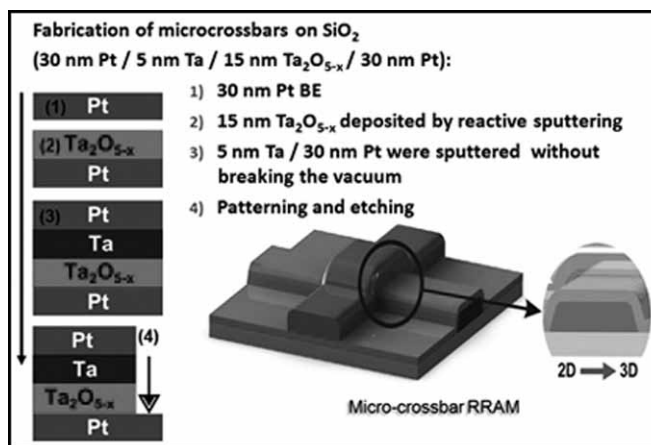


Figure 2: Outline of the device fabrication process for TaO_x devices.

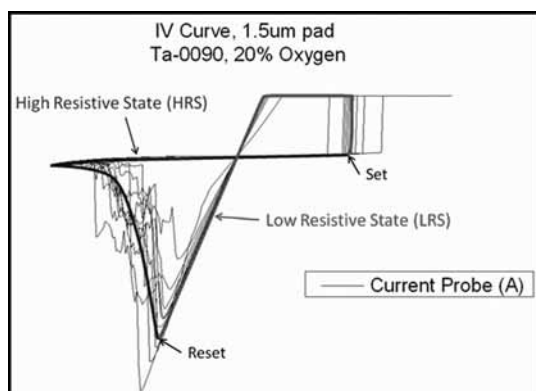


Figure 3: Quasistatic IV curve of a specific trial. Note the two resistive states as well as the set and reset voltage for this stable switching. The plateau arises from the current compliance of the system.

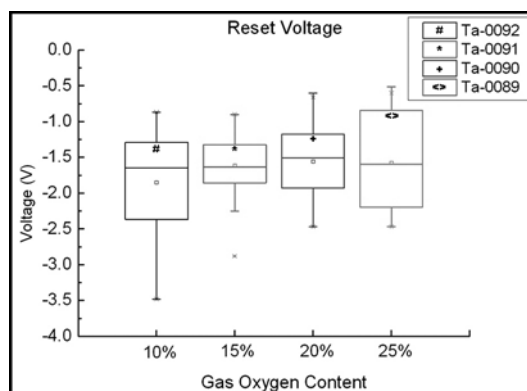


Figure 4: Reset voltage versus oxygen content during sputtering. No apparent relationship between the two.

ran one forming cycle from 0 to 4 volts with a step size of 30 mV, a hold time of 30 ms and a current compliance of 0.2 mA. Then ten set-reset cycles were run with a max voltage of 3.5V, a minimum voltage of -2V, a step size of 30 mV, hold time of 30 ms and a 0.2 mA current compliance up and 20 mA current compliance down. This process was then done on each possible device on the sample totaling about 100 devices per sample depending on availability of the autoprobe.

Results:

Overall there was stable switching of the TaO_x devices. One device example is shown in Figure 3. This allowed for median set, reset and forming voltages to be gathered from the data sets. Ultimately there was no overall trend with set, reset or forming voltages and the changing oxygen contents of the devices as shown in Figure 4. The median set voltage was about 2V, the median reset voltage was about -1.75V and the median forming voltage was about 2.5V with only minor changes with different oxygen content.

Discussion and Future Work:

In the end, the oxygen content during sputtering and sample preparation had no effect on the switching characteristics, which shows that the filamentary mechanism is fully in-

dependent of different oxygen content during deposition. In the future, examination of other materials may be worthwhile such as TiO_x in order to see if this oxygen independence during sample deposition is specific to TaO_x or is due to the filamentary mechanism.

Acknowledgements:

I would like to acknowledge the National Nanotechnology Infrastructure Network and their International Research Experience for Undergraduates (iREU) Program, the National Science Foundation and the Jülich Forschungszentrum for allowing me this great opportunity. I would also like to thank my principal investigator, Regina Dittmann, my mentor, Katharina Skaja, and my colleague, Benedikt Arndt. Each of them both helped me in my research and aided me in feeling welcome during my stay in Germany. I would also like to thank my entire lab group for their fantastic suggestions about where I should travel and what to do while there.

References:

- [1] R. Waser, et al. Nanoelectronics and Information Technology, Chapter 30, Wiley-VCH, 2012. Print.
- [2] C. Lee, et al. IEEE Elec. Dev. Lett, 32 399-401 (2011).
- [3] A. Sawa, Materials Today, 11 28-36 (2008).

Understanding Magnetic Plasmon Mode Mixing Using Electron Energy Loss Spectroscopy

Harrison J. Goldwyn

Physics, University of California Santa Barbara

NNIN REU Site: NanoTech User Facility, University of Washington, Seattle, WA

NNIN REU Principal Investigator: David J. Masiello, Chemistry, University of Washington

NNIN REU Mentor: Nicholas W. Bigelow, Chemistry, University of Washington

Contact: harrisongoldwyn@gmail.com, masiello@u.washington.edu, nicholas.bigelow@gmail.com

Abstract:

Circular clusters of gold nanoparticles (Au NPs) support collective magnetically characterized plasmons. Because of their low energy loss and phase dependent bonding characteristics, magnetic plasmons show potential for use in sub-wavelength optical circuitry [1] as well as artificial conjugated molecules [2]. In order to utilize magnetic plasmons in application, a detailed understanding of the mode mixing involved must be developed. Because nanoparticle clusters that support magnetic plasmons are composite, their mode structures are inevitably complex. This project began as a pursuit to describe the fundamental oscillatory modes of some magnetic plasmon supporting systems using electron energy loss spectroscopy (EELS). Over time, the project evolved and focus shifted to a specific structure with interesting magnetic modes capable of being described using the language of hybridized molecular orbital theory.

Computational Method:

All simulations were accomplished using an in-house modified version of Bruce T. Draine's Discrete Dipole Approximation code (DDSCAT) [3]. The DDA approximates a scatterer as a Cartesian grid of polarizable points. The polarization at grid location j is determined by the incident field and the induced fields of all grid points $\neq j$. Polarizations of all grid points form a coupled system of equations that can be solved iteratively to convergence. Our version of the DDA incorporates the electron beam as a field source (eDDA) [4]. The eDDA expands our observation of scattering objects because it is an experimentally viable local field source.

Magnetic Plasmon and EELS:

The magnetic plasmon referenced is actually a coherent excitation of circularly polarized electric dipole plasmons. The oscillating electric dipoles form oscillating currents in the structures that support this plasmon (see Figures 1 and 2). These oscillating currents give rise to oscillating magnetic dipoles that characterize the oscillatory mode of interest.

While stimulating the magnetic plasmon mode with an electron-beam (e-beam) requires careful consideration of symmetry, it also allows access to modes not accessible by plane-wave light. In order to stimulate the circular polarizations necessary to mediate alternating currents, the system of particle cluster and beam must possess the proper symmetry.

For the Decamer structure shown in Figure 1, a pair of alternating currents can be stimulated by position of the e-beam very close the outer edge of one of the center particles. The passing electron polarizes the close

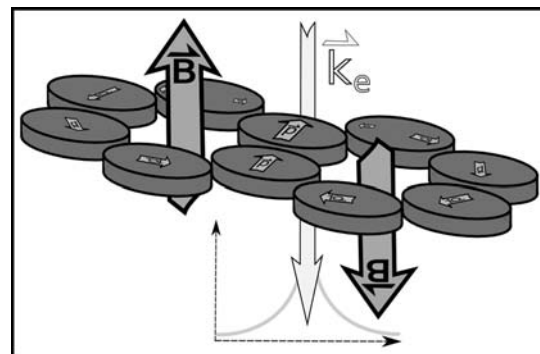


Figure 1: Correct stimulation of magnetic plasmon in decamer using the e-beam. Individual cylinder electric dipole plasmons are shown using polarization arrows (defined negative to positive).

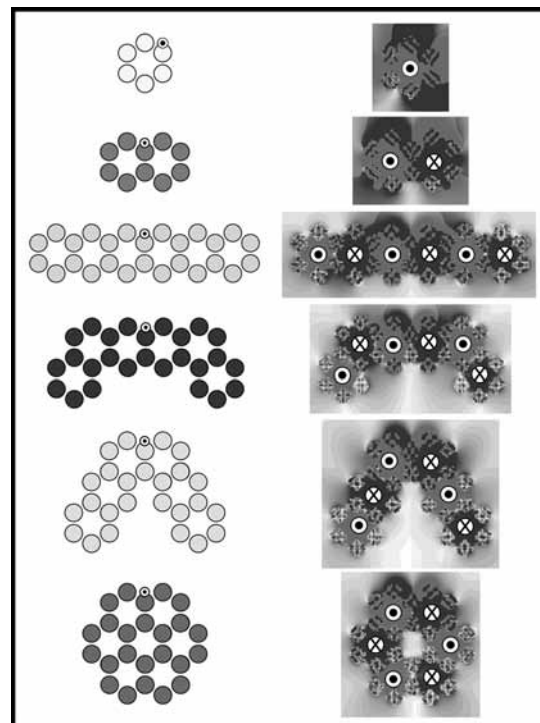


Figure 2: In case of greyscale printing, the magnetic field direction will be marked qualitatively. Beam location is marked per structure. (See full-color version on inside cover.)

center particle more than its pair of symmetric neighbors; thus, alternating currents propagate around the two hexamers and two opposing magnetic dipoles begin to oscillate.

Magnetic Plasmon in Various Structures:

Using the simulation methods described above, we confirmed the existence of the magnetic plasmon in six conjugated hexamer structures (relatively normalized field plots seen in Figure 2). For all structures, the hexamer subunit consists of six gold cylinders (260 nm diameter, 80 nm height) — each pair separated by 30 nm. Although the e-beam excitation was local, the magnetic plasmon propagated through neighboring hexamer sub-units, making the magnetic plasmon useful for sub-wavelength optical circuitry.

The EELS for all six structures is shown in Figure 3. Although all six structures supported the same scattered magnetic field in the same spectral range, their EEL spectra were very different. Instead of seeing a spectral peak normally characteristic of a resonance, we saw steep Fano-like line shapes. At that point we could only assume that these obscure shapes were caused by Fano-like interference of the normal oscillatory modes. If this was the case, the spectra imply extremely complicated mode interference.

Artificial Conjugated Molecules:

Now that we understood when and where magnetic plasmons would arise, we began to describe the fundamental mode mixing that was occurring below the surface. In order to avoid the reality of our extremely complicated system of coupled oscillators (the billions of electrons), we decided to model the system as only interactions between neighboring magnetic dipoles. This simplified system is already well understood using molecular Huckel Theory. The task was complicated by the fact that our benzene equivalent structure had less symmetry than molecular benzene.

Future Work:

So far, our model describes the two lower energy magnetic modes that appear in our benzene analog (shown in Figure 4) as combinations of three benzene molecular states. We will continue to access our structures for use as molecular models by showing existence of the remaining benzene modes.

Acknowledgements:

David Masiello, Nicholas Bigelow, Mack Carter, the NNIN REU Program, and NSF.

References:

- [1] N. Liu, et al. Manipulating Magnetic Plasmon Propagation in Metallic Nanocluster Networks. *ACS Nano* 6, 5482 (2012).
- [2] N. Liu, et al. Magnetic Plasmon Formation and Propagation in Artificial Aromatic Molecules. *Nano Lett.* 12, 364 (2012).
- [3] B. T. Draine. The Discrete-Dipole Approximation and Its Application to Interstellar Graphite Grains. *The Astrophysical Journal*, 333:848-872, 1988 October 15.
- [4] N.W. Bigelow, et al. Signatures of Fano Interferences in the EELS and Cathodoluminescence of Symmetry-Broken Nanorod Dimers. *ACS Nano* 2013 7 (5), 4511-19.

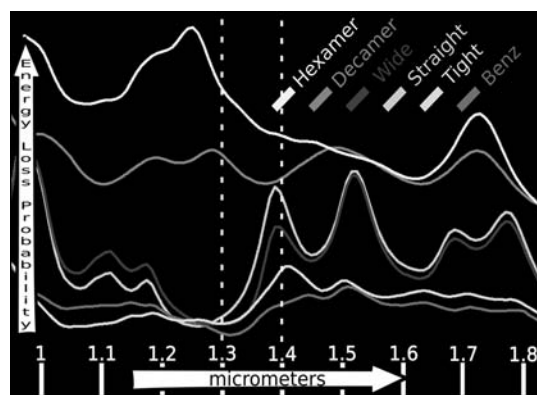


Figure 3: EELS for all six structures.

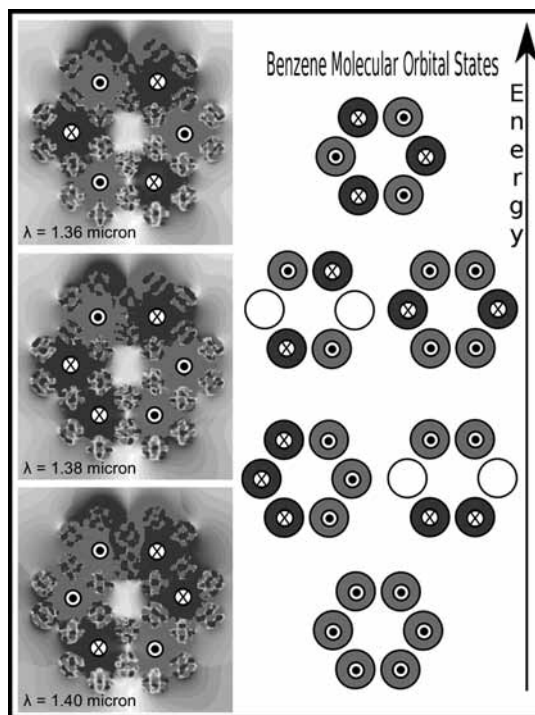


Figure 4: The two lower energy magnetic modes that appear in our benzene analog.

Mobile Targeted Objects Steered by Chemical Micropumps

Kyle Marshall

Chemical Engineering, The University of Arizona

NNIN REU Site: Penn State Nanofabrication Laboratory, The Pennsylvania State University, University Park, PA

NNIN REU Principal Investigator: Dr. Darrell Velegol, Chemical Engineering, The Pennsylvania State University

NNIN REU Mentor: Abhishek Kar, Chemical Engineering, The Pennsylvania State University

Contact: kpm1@email.arizona.edu, velegol@enr.psu.edu, ayk5241@psu.edu

Abstract:

Catalytic nanomotors are bimetallic nanorods that move spontaneously in a solution of hydrogen peroxide (H_2O_2). However, these nanomotors move in random pathways. This research aimed to steer these nanomotors using chemical micropumps, such as calcium carbonate ($CaCO_3$) microparticles, which generate radial diffusioosmotic flows. Here we have shown a nanorod moving with directionality using three $CaCO_3$ micropumps. We also investigated the fabrication of a large, tunable array of micropumps by growing $CaCO_3$ in microwells on a lithographed, PDMS surface. Currently the method of growing $CaCO_3$ in this array of microwells is being refined and we hope to eventually use this method to steer nanorods in strategically-patterned arrays.

Introduction:

In our lab, we study micron-sized particles, such as gold platinum (AuPt) nanorods, that spontaneously move in a solution of H_2O_2 , as shown in Figure 1. The movement of these nanorods in H_2O_2 occurs due to a phenomenon known as autoelectrophoresis. The catalytic reaction of H_2O_2 around the bimetallic nanorods creates a self-generated electric field, which then propels the nanorods forward [1]. Recently it has been found that chemical micropumps operate under a similar phenomenon known as autodiffusiophoresis. The dissolution of salt microparticles, such as $CaCO_3$, in an aqueous solution generates radial electric fields due to differences in the diffusion rates of the dissolved ions. Depending on the direction of the electric field and the charge of the mobile objects in solution, objects can be pulled toward these micropumps. Once the mobile objects are near the micropumps, radial diffusioosmotic flows sweep these objects along the charged surface of the substrate on which the micropumps rest, as shown in Figure 2 [2].

The spatiotemporal nature of the micropumps creates exclusion regions around the pumps where we predict the movement of catalytic nanomotors will be restricted. We envision that a strategically-patterned surface of $CaCO_3$ micropumps could direct nanomotors by making them move orthogonal to the radial flows of the micropumps.

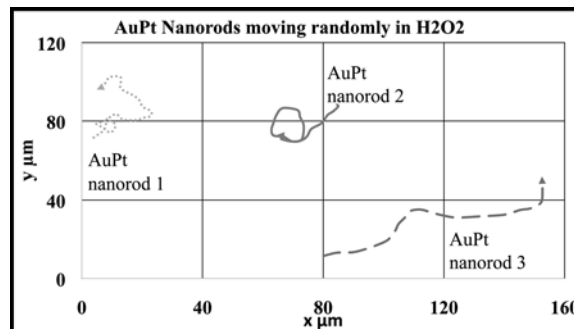


Figure 1: Graph showing the simultaneous, spontaneous movement of AuPt nanorods in a H_2O_2 solution.

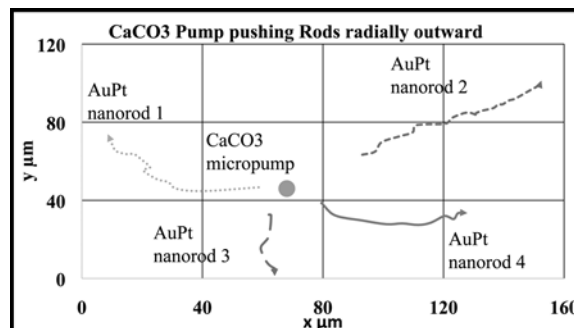


Figure 2: Graph showing AuPt nanorods moving radially away from a $CaCO_3$ micropump.

Therefore, our research question was: can we start with the random pathways of the catalytic nanomotors and get more directionality by strategically placing an array of micropumps around these nanomotors?

Experimental Procedure:

AuPt nanorods were obtained from the Chemistry Department at Penn State. $CaCO_3$ microparticles of roughly 7-10 μm were made through a precipitation synthesis. A solution of 0.33 M calcium chloride ($CaCl_2$) was added to a 0.33 M solution of sodium carbonate (Na_2CO_3), and after minutes of vigorous

stirring, the solution was washed with deionized water. Diluted CaCO_3 microparticles and AuPt nanorods in deionized water were added on top of a borosilicate glass slide. A standard microscope was used to capture images and videos at 10 \times -50 \times magnification.

An array of microwells in a polydimethylsiloxane (PDMS) surface was made by using standard photo- and soft-lithography on a Karl Suss MA/BA6 contact aligner [3]. CaCO_3 was grown in the microwells by first passing a CaCl_2 solution horizontally over the microwells. Then after evaporation of this first solution, a solution of Na_2CO_3 was passed horizontally over the microwells and removed after about ten minutes.

Results and Conclusions:

The random pathway of the catalytic nanomotors and the radial pumping of the CaCO_3 can be observed in Figure 1 and Figure 2, respectively. When adding a second CaCO_3 microparticle and H_2O_2 , the movement of the nanomotors was still largely haphazard. However, the spacing of the micropumps in this system may need to be further fine-tuned in order to obtain more directionality by limiting the degree of freedom in the movement of the nanorods.

When adding a third CaCO_3 and taking away H_2O_2 , a single AuPt nanorod not only moved without H_2O_2 , but also moved in a linear path away from the chemical micropumps, as shown in Figure 3. This is the key result of this research and shows that AuPt nanorods can be steered at a local level by chemical micropumps. This system is also important because it may allow for other charged objects to be steered, not just nanomotors.

Figure 4 shows a dark formation, which is believed to be CaCO_3 , in one 15 μm well of an array of microwells on a PDMS surface. Growing CaCO_3 in an array of microwells on a PDMS surface is a promising method to make large, tunable arrays of chemical micropumps.

Future Work:

We hope to further refine the growing method in order to produce large, tunable arrays of micropumps to study long-range, directed motion as well as directed motion with strategic patterns. In the future, comparison of the experimental data to mathematical models of the flows could also give insight to the specific mechanisms by which the chemical micropumps move and steer the nanorods.

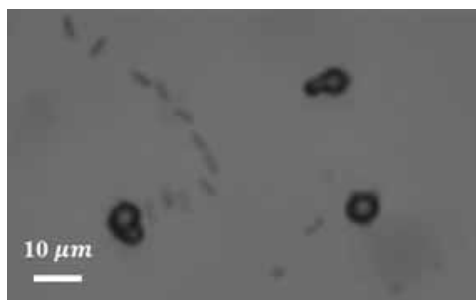


Figure 3: Time lapse image showing a single AuPt nanorod moving with directionality by the radial pumping of three CaCO_3 micropumps.

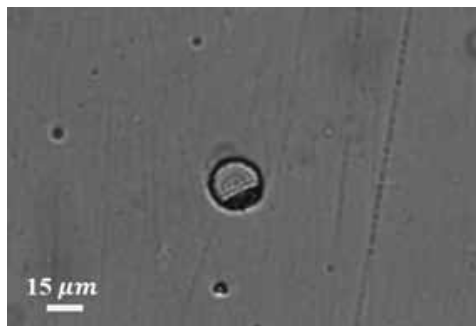


Figure 4: An image of a dark formation, which is believed to be CaCO_3 , in a 15 μm well on a PDMS surface.

Acknowledgements:

I would like to thank Dr. Darrell Velegol and Abhishek Kar for having me in their lab this summer, Antonio Romero, Flory Wong, and Dr. Ayusman Sen in the Chemistry Department at Penn State for their collaboration on this project, Kathleen Gehoski and the Penn State Nanofabrication Laboratory staff for their support and help, the NNIN REU Program for organizing this undergraduate research experience, and the National Science Foundation for funding.

References:

- [1] W. F. Paxton, P. T. Baker, T. Kline, Y. Wang, T. E. Mallouk, and A. Sen. *Journal of the American Chemical Society*, 128, 14881-14888 (2008).
- [2] J. J. McDermott, A. Kar, M. Daher, S. Klara, G. Wang, A. Sen, and D. Velegol. *Langmuir*, 28, 15491-15497 (2012).
- [3] D. Qin, et al. *Nature Protocols*, 5.3, 491-502 (2010).

Fabricating Nanostructures to Modulate Local Potential in Graphene

Kenton McFaul

Applied Physics, Grove City College

NNIN REU Site: Penn State Nanofabrication Laboratory, The Pennsylvania State University, University Park, PA

NNIN REU Principal Investigator: Dr. Jun Zhu, Department of Physics, The Pennsylvania State University

NNIN REU Mentor: Jing Li, Department of Physics, The Pennsylvania State University

Contact: mcfaulkj1@gcc.edu, jzhu@phys.psu.edu, jil5369@psu.edu

Abstract and Introduction:

Graphene is an atomically thin allotrope of carbon with unique electrical properties. Its high carrier mobility at room temperature and ultra-high thermal conductivity make it a promising material for nanoscale circuit applications. One way to study the nanoscale transport properties of ballistic graphene p-n junctions is to modulate the local potential with lithographic gates that are several tens of nanometers in scale. Lithography can also be used to build graphene nanoribbon (GNR) arrays, which lead to a method to build radio frequency amplifiers.

Our efforts were directed at fabricating GNR arrays and gold split-gates with length scales less than 100 nm. After performing electron-beam lithography, we developed our patterns at low temperatures using an ice bath. Oxygen reactive ion etching (RIE) was employed to etch the graphene into nanoribbon arrays, and electron gun evaporation was used to deposit the gold split-gate electrodes, followed by a lift-off process. In order to optimize the recipe, variables such as resist type, electron beam dose, developer type, and development time were systematically tested. We successfully fabricated nanoribbon arrays with a period of 100-180 nm using poly(methyl methacrylate) (PMMA) as the e-beam resist, and arrays with a period of 60-80 nm using ZEP. We successfully fabricated split-gates separated by 50-90 nm using PMMA/MMA bilayer resist.

Procedure and Results:

We fabricated our nanoribbon arrays with a layer of graphene grown using chemical vapor deposition (CVD). The CVD graphene was transferred onto a silicon wafer with a thin layer of thermally grown silicon oxide. Our first batch of samples was made with PMMA 950K A3 as resist. Electron-beam lithography was used to pattern arrays of nanoribbons using doses ranging from 300-400 $\mu\text{C}/\text{cm}^2$. The nanoribbons we patterned were 20-90 nm wide, separated by a distance equal to their width.

Both MIBK: IPA 1:1 and MIBK: IPA 1:3 were used as developers to test the influence of concentration on feature resolution. Developer with a higher concentration of IPA requires a longer time to develop, but provides finer control. We developed our samples at temperatures below 10°C by immersing our developer in an ice bath. Cold development is known to increase the resolution of nanostructures [1]. Finally, oxygen RIE was employed to etch the graphene into nanoribbons.

With PMMA as a resist, we successfully formed GNR arrays with periods from 100-180 nm at a dose of 400 $\mu\text{C}/\text{cm}^2$. However, arrays with periods from 40-80 nm were either over-etched or completely gone, revealing a fundamental limit of our process using PMMA. We also found that a higher concentration of IPA did not increase the resolution of our nanoribbons; it only slowed down the process, and our samples were underdeveloped.

Electron scattering during e-beam lithography produced exposed stripes that were wider than the intended size, resulting in the overetching of graphene. Reducing this effect was critical at scales less than 100 nm. In order to obtain nanoribbons narrower than 50 nm, we chose ZEP 520a as our resist for the second batch of GNR arrays because of its high contrast and resolution [2]. We also wrote our features smaller than the intended size to compensate for the scattering effect. Doses from 270-390 $\mu\text{C}/\text{cm}^2$ were tested. We developed the arrays in cold n-amyl acetate. With ZEP as the resist, we successfully formed GNR arrays with periods from 60-80 nm at doses of 270-350 $\mu\text{C}/\text{cm}^2$.

We fabricated our gold split-gates on a silicon wafer, and used electron beam lithography to pattern gates that were separated by 50-200 nm. ZEP 520a, which is known to have an inherent undercut [3], and conventional PMMA/MMA bilayer resist were tested.

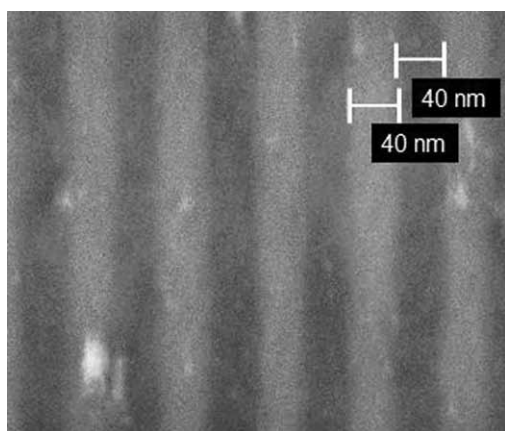


Figure 1: 80 nm period nanoribbon array made with ZEP.

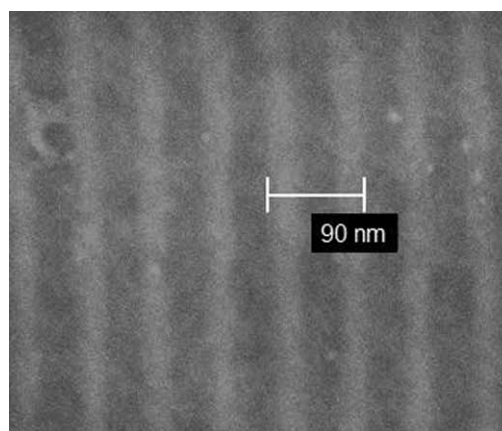


Figure 2: 60 nm period nanoribbon array made with ZEP.

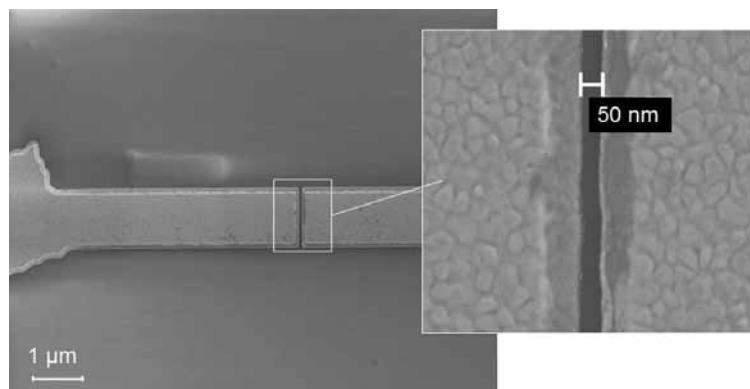


Figure 3: 50 nm split-gate made with a PMMA/MMA bilayer.

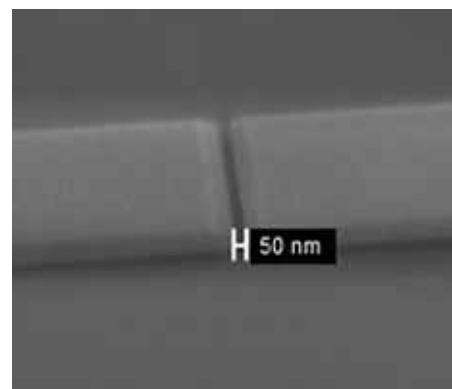


Figure 4: 50 nm split-gate made with a PMMA/MMA bilayer.

The split-gates fabricated using ZEP were written with doses from 250-390 $\mu\text{C}/\text{cm}^2$, and developed in n-amyl acetate below 10°C. We deposited 50 nm of gold with e-gun evaporation, and performed metal lift-off in a heated bath of Remover PG (75-85°C). Scanning electron microscope images and resistance measurements revealed that split-gates 90 nm wide and above were successful, but smaller gates either shorted or had very rough edges.

PMMA/MMA bilayer resist yielded much cleaner results. We wrote the patterns with doses from 300-450 $\mu\text{C}/\text{cm}^2$, and developed in cold MIBK: IPA 1:1. Metal lift-off was performed using acetone. Because of electron scattering, the split-gates were much thinner than the pattern size. This was the desired effect, and split-gates written at 70-90 nm had a final size less than 50 nm.

Conclusions:

It is possible to fabricate nanoscale GNR arrays and local gate structures using our processes. We achieved 30 nm ribbons using ZEP, correcting for electron scattering, and developing in an ice bath. Split-gates with a separation of 50 nm were achieved by writing 70-90 nm gate structures in PMMA/MMA

bilayer resist. With these structures and techniques, researchers can further study the transport properties of graphene by locally modulating the potential.

Acknowledgments:

I would like to thank Professor Jun Zhu for her advice and the use of her lab. I would also like to thank Jing Li for putting in many hours to teach me and help me with this project. I also greatly appreciate the Zhu Group and the Penn State Nanofab Staff for all the advice, and the National Nanotechnology Infrastructure Network REU Program, along with the National Science Foundation, for providing funding.

References:

- [1] Cord, B., et al., "Optimal temperature for development of poly(methylmethacrylate)." *Journal of Vacuum Science and Technology B*, 25, 2013-2016 (2007).
- [2] Chapin, C., et al., "Optimization Studies of ZEP520." Georgia Institute of Technology, Nanotechnology Research Center, 2010. PowerPoint.
- [3] Conway, J., "E-beam Process for ZEP-520A to be used for Metal Liftoff and RIE." Stanford University, SNF, 2005. Web.

Tungsten Silicide Films for Superconducting Resonators

Kiwamu Nishimoto

Solid State Physics, Tohoku University, Sendai, Japan

NNIN iREG Site: UCSB Nanofabrication Facility, University of California, Santa Barbara, CA

NNIN iREG Principal Investigator: Professor Benjamin Mazin, Department of Physics, University of California, Santa Barbara

NNIN iREG Mentor: Dr. Gerhard Ulbricht, Department of Physics, University of California, Santa Barbara

Contact: a8tb1191@mail.tagen.tohoku.ac.jp, bmazin@physics.ucsb.edu, ulbricht@physics.ucsb.edu

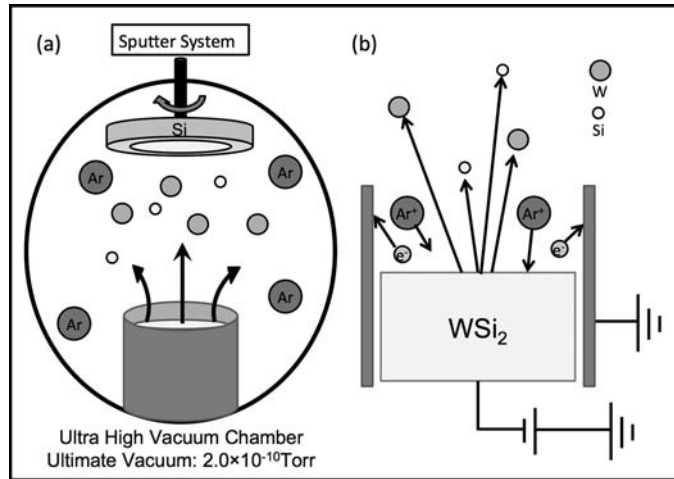


Figure 1: Schematic illustration of (a) the way to deposit WSi₂, and (b) the way to sputter WSi₂.

Abstract:

We have started to examine tungsten silicide (WSi₂) as a possible candidate for microwave kinetic inductance detectors (MKIDs). WSi₂ for MKIDs has to have a suitable critical temperature (T_c) that is uniform over the wafer and very low (about 1-2K), and the films should have low stress. We explored the parameter space of the WSi₂ sputter deposition to find the ideal condition. We used the sputter system located in the cleanroom in order to deposit WSi₂ on silicon (Si) wafers in ultra-high vacuum. We deposited WSi₂ at base pressures below 1.0×10^{-8} Torr on rotating Si wafer (30 rpm) by creating an argon (Ar) plasma above the WSi₂ target. We measured the thickness by using scanning electron microscopy (SEM), and the T_c and the room temperature resistivity of our deposited WSi₂ films.

Introduction:

MKIDs are promising for astronomy because these detectors provide highly multiplexed arrays of detectors that can be configured to operate from the sub-millimeter to the x-ray regime [1]. These detectors allow us to determine the energy

and arrival time of individual photons. The applications of this technology ranges from detecting earth-like planets around nearby stars to untangling the emission mechanisms of pulsars.

In its simplest form, a MKID consists of a thin film superconductor patterned into a resonator [1]. When a photon is absorbed in the superconductor, it breaks Cooper pairs, creating an excess of non-equilibrium quasiparticles [1]. This excess of quasiparticles alters the complex surface impedance of the superconductor, raising the kinetic inductance and surface resistance, which causes the resonance feature to shift to a lower frequency and broaden [1]. MKIDs are generally operated at temperatures well below the superconducting transition in order to minimize the thermal population of quasiparticles. To achieve good sensitivity, the T_c of MKID resonator metal (WSi₂) needs to be around 1-2K. In this instance, the target value of T_c is 1-2K. It is known that T_c is different depending on the Si content of WSi₂. Therefore the T_c of sputtered thin film WSi₂ can be controlled by deposition conditions.

Experimental Procedure:

The experiment was conducted in an ultra high vacuum chamber. We sputtered a high purity WSi₂ target by creating DC plasma above the WSi₂ in Ar atmosphere. Si wafer was rotated during experiment so that we could deposit homogeneous WSi₂ over a 3-inch wafer. Varying the parameter space of the WSi₂ sputter deposition (power, Ar pressure, Ar flow, coat time) allowed to control the W:Si ratio. We measured the thickness by using SEM, and the T_c and the room temperature resistivity of our deposited WSi₂ films.

Results and Conclusions:

First, we prepared three pieces from different locations of a 3-inch wafer after deposition to measure the film thickness and T_c , so that we could verify that there are not any morphological differences of WSi₂ over a 3-inch wafer; shown in Figure 2. Position means the distance from center of the wafer. From this data, we could show that T_c did not change depending on the position of the wafer. So, we do not have to worry about the homogeneity of WSi₂.

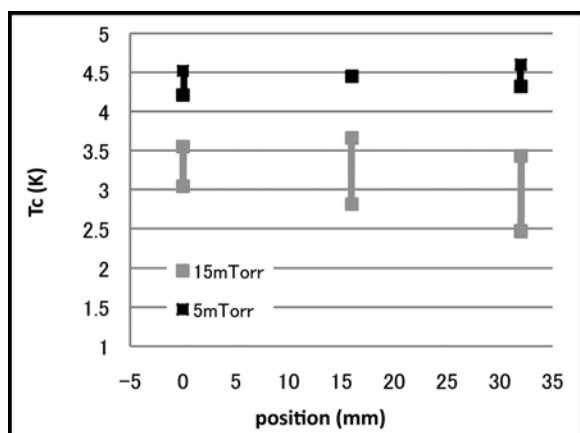


Figure 2: T_c depending on position of the wafer. (Ar flow: 20 sccm, power: 120W).

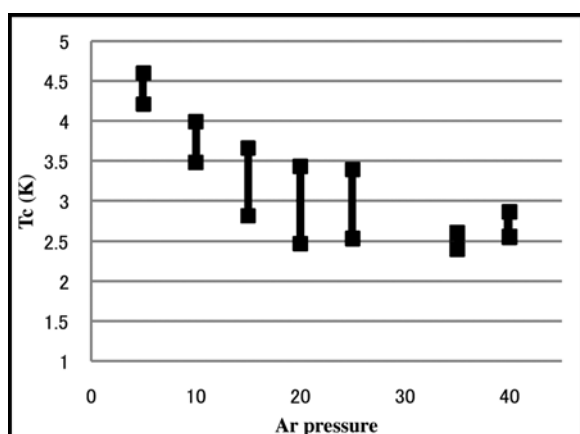


Figure 3: T_c depending on Ar pressure. (Ar flow: 20 sccm, power: 120W).

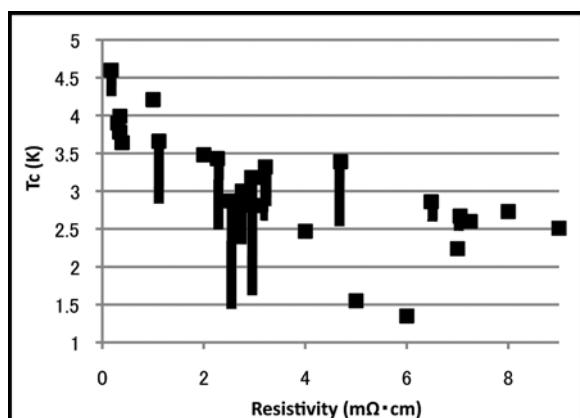


Figure 4: T_c relationship with resistivity. Resistivity was calculated with surface resistivity and thickness.

Figure 3 shows that by varying the Ar pressure T_c of $W\text{Si}_2$ can be minimized. It is guessed that high Ar pressure results in a low Si content in $W\text{Si}_2$, because Si is lighter than W and, therefore, tends to be scattered by Ar atom and ion more than W. T_c of $W\text{Si}_2$ depends on stoichiometry and was mapped by Kondo [2] for transition temperatures above 1.9K. For both very small and large Si concentrations, the T_c falls below 1.9K, but for Si atomic percentages ranging from $\sim 7\%$ up to $\sim 60\%$, the T_c rapidly rises up to 5K, with a maximum T_c for Si atomic percentages between 20 and 40%. We guess that higher the Ar pressure becomes, the lower the Si content becomes, but there is a limit a parameter of Ar pressure to minimize Si content. We also got several data of T_c depending on Ar flow, power and coat time but those are not sufficient to discuss.

By measuring resistivity at room temperature, we intended to predict T_c . We wanted to do that because it takes many hours to measure T_c . From previous research, it is known that high resistivity implies low T_c . Figure 4 shows the relationship between T_c and the room temperature resistivity. From the graph, the sample has high resistivity tends to get low T_c . We guessed it is possible to predict if T_c is high or low by room temperature resistivity.

Acknowledgments:

I would like to thank Professor Ben Mazin, Gerhard Ulbricht, Mazin laboratory members for their exceptional guidance, Peter Duda, Lizzie Slaughter for their expertise, and Samantha Cruz for her advice as program coordinator. Finally, I would like to acknowledge and thank the National Nanotechnology Infrastructure Network International Research Experience for Graduates (NNIN iREG) Program and the National Institute for Material Science for funding this project.

References:

- [1] T. Cecil, A. Miceli, O. Quaranta, C. Liu, D. Rosenmann, S. McHugh, and B. Mazin, *Appl. Phys. Lett.* 101, 032601 (2012).
- [2] S. Kondo, *J. Mater. Res.* 7, 853-860 (1991).

Electrical Characterization of GaAs/InAs Core/Shell Nanowires and InAs Nanotubes

Jordan Occeña
Engineering Physics, University of Tulsa

NNIN iREU Site: Institut Für Bio- Und Nanosysteme (IBN), Forschungszentrum, Jülich, Germany
NNIN iREU Principal Investigator: Dr. Mihail Ion Lepsa, Peter Grünberg Institute 9, Forschungszentrum Jülich
NNIN iREU Mentor: Torsten Rieger, Peter Grünberg Institute 9, Forschungszentrum Jülich
Contact: jordan-occeña@utulsa.edu, m.lepsa@fz-juelich.de, t.rieger@fz-juelich.de

Introduction:

Semiconductor nanowires (NWs) show promise for a variety of nanoelectronic applications due to their high surface area to volume ratio and two-dimensional confinement of charge carriers. The properties of these NWs can be further manipulated through the formation of radial heterostructures. In particular, the use of a gallium arsenide (GaAs) NW core to support an indium arsenide (InAs) shell can potentially result in a tubular conductor suitable for high performance field effect transistors (FETs). The GaAs core can later be removed by selective etching, resulting in an InAs nanotube. Due to its additional surface area and the relaxation of dislocations associated with the GaAs/InAs interface, it is expected that the mobility (μ_{FE}) of this InAs nanotube would exceed that of the core/shell NW. Here, we investigate and compare the resistivity (ρ), electron concentration (n_e), and μ_{FE} of GaAs/InAs core/shell NWs and InAs nanotubes.

Experimental Procedure:

The core/shell NWs studied were grown by molecular beam epitaxy as described by Rieger, et al. [1]. NWs were grown with three different core diameters/shell thicknesses: 110 nm/15 nm, 110 nm/22 nm, 150 nm/18 nm.

In order to extract ρ , n_e , and μ_{FE} , top-gate NW FETs were fabricated with hafnium oxide (HfO_2) as the gate dielectric and GaAs/InAs core/shell NWs as the channel. Core/shell NWs were first coated with 10 nm of HfO_2 by atomic layer deposition. The NWs were then mechanically transferred to a substrate consisting of 200 nm of silicon oxide on degenerately doped silicon.

Optical microscope images of the distribution of the transferred NWs were used to design source, drain, and top-gate contacts for selected NWs. Electron-beam lithography was used to define 1 μm long Ti/Au top-gates, which were deposited by electron beam evaporation. After gate deposition, the HfO_2

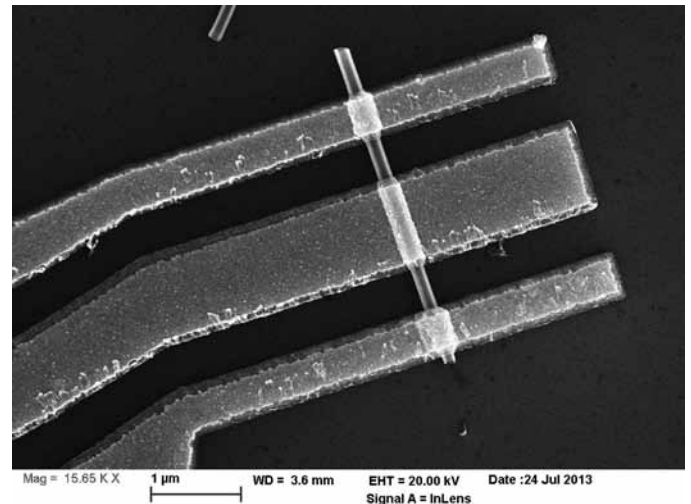


Figure 1: Top-view SEM image of an InAs nanotube FET.

dielectric was removed from the source and drain regions of the NW using a three minute wet etch in 0.05% hydrofluoric acid. Source and drain contacts were then patterned and deposited in the same way as the top-gate contacts. The spacing between adjacent contacts was 500 nm. The electrical properties of the NWs were characterized by two-, three-, and four-probe current-voltage (I-V) measurements on the NW FETs.

After characterization of the core/shell NWs was complete, the GaAs core was selectively etched with a 1:1:40 mixture of $\text{NH}_4\text{OH}:\text{H}_2\text{O}_2:\text{H}_2\text{O}$ for five minutes to obtain InAs nanotubes, while leaving the FETs intact. Electrical measurements were then repeated for the nanotube FETs. Scanning electron microscope (SEM) images of the nanotube FETs were taken after electrical characterization (Figure 1).

Equation 1: $\rho = \frac{RA}{L}$

Equation 2: $C = \frac{2\pi\epsilon_0\epsilon_r L}{\ln\left[\frac{t_{ox}}{r} + 1 + \sqrt{\left(\frac{t_{ox}}{r}\right)^2 + 2\frac{t_{ox}}{r}}\right]}$

Equation 3: $n_{el} = -\frac{CV_{th}}{eLA}$

Equation 4: $\mu_{FE} = \frac{g_m L^2}{V_{SD} C}$

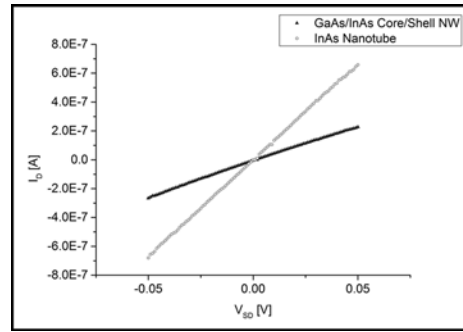


Figure 2: Exemplary two-probe I-V characteristics of a core/shell NW vs. nanotube.

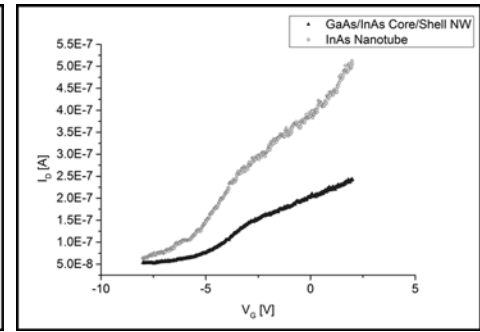


Figure 3: Exemplary three-probe ID-VG characteristics of a core/shell NW vs. nanotube.

The resistivity of each NW and nanotube was determined by two-probe measurements using Equation 1, where L is the length of the NW between source and drain, R is the resistance of the NW taken from the I-V curve, and A is the portion of the cross-sectional area of the NW that conducts, which is limited to the InAs shell in core/shell NWs due to the band alignment of GaAs and InAs [2]. A small number of four-terminal devices were fabricated to measure the contact resistance, which was found to be negligible in comparison to the resistance of the NWs and was not included in calculations of ρ .

Values for n_e and μ_{FE} were extracted from three-probe measurements according to Equations 3 and 4, where C is the gate capacitance, V_{th} is the threshold voltage from the I_D - V_G curve, e is the electron charge, g_m is the transconductance from the I_D - V_G curve, and V_{SD} is the voltage between the source and drain, which was held constant at 0.02 V for all three-probe measurements. The gate capacitance, C , was approximated using Equation 2, which is the general form of the gate capacitance for a back-gate NW FET, where ϵ_0 is the vacuum permittivity, ϵ_r is the relative permittivity of the gate oxide, t_{ox} is the gate oxide thickness, and r is the NW radius. To account for the use of a top-gate instead of a back-gate, the capacitance values calculated by Equation 2 were increased by 14%, as suggested in Dayeh et al. [3].

Results and Discussion:

For forty-one GaAs/InAs core/shell NWs tested, an average ρ of 0.14 $\Omega\cdot\text{cm}$ was found. After etching of the NW cores to obtain InAs nanotubes, the average ρ decreased to 0.05 $\Omega\cdot\text{cm}$. An example of two-probe I-V curves for one device before and after etching of the core is shown in Figure 2.

For twenty-nine core/shell NW FETs on which three-probe measurements were conducted, an average n_e of $1.33 \times 10^{19} \text{ cm}^{-3}$ and average μ_{FE} of $19.2 \text{ cm}^2(\text{V}\cdot\text{s})^{-1}$ were found. The same devices, after etching of the GaAs core, exhibited an average n_e of $1.41 \times 10^{19} \text{ cm}^{-3}$ and an average μ_{FE} of $32.0 \text{ cm}^2(\text{V}\cdot\text{s})^{-1}$. Sample three-probe I_D - V_G curves are shown in Figure 3. For all the parameters, the data showed a large spread most likely related to the device processing.

It was expected that the removal of the GaAs core would allow for the formation of donor-type surface states on the inner surface of the InAs nanotubes in addition to those already present on the outer surface, thus increasing n_e and decreasing ρ . The lack of a significant increase in n_e found experimentally suggests the possible formation of InGaAs at the GaAs/InAs interface. Meanwhile, the small increase in μ_{FE} and decrease in ρ found might still be attributed to relaxation of dislocations associated with the GaAs/InAs interface.

Acknowledgements:

A special thanks to Dr. Mihail Ion Lepsa and Torsten Rieger for their guidance and support, as well as to my colleagues at the Forschungszentrum Jülich and the coordinators of the NNIN iREU Program. Thanks also to the NSF for funding this work.

References:

- [1] Rieger, T., et al. Nano Letters, 12(11), 5559-64.
- [2] Blömers, C., et al. Nanotechnology, 24(3), 035203.
- [3] Dayeh, S., et al. Small, 3(2), 326-32.

Current-Voltage Characterization and Two-Step Photocurrent Generation in Lattice-Matched Quantum Dot Solar Cells

Adam Christopher Overvig
Engineering Physics, Cornell University

NNIN iREU Site: National Institute for Materials Science (NIMS), Tsukuba, Ibaraki, Japan

NNIN iREU Principal Investigators: Dr. Takeshi Noda, High Efficiency Solar Cell Group, National Institute for Materials Science, Ibaraki, Japan;
Dr. Hiroyuki Sakaki, Toyota Technological Institute, Nagoya, Japan

NNIN iREU Mentor: Dr. Martin Elborg, High Efficiency Solar Cell Group, National Institute for Materials Science

Contact: aco2124@columbia.edu, noda.takeshi@nims.go.jp, sakaki.hiroyuki@nims.go.jp, elborg.martin@nims.go.jp

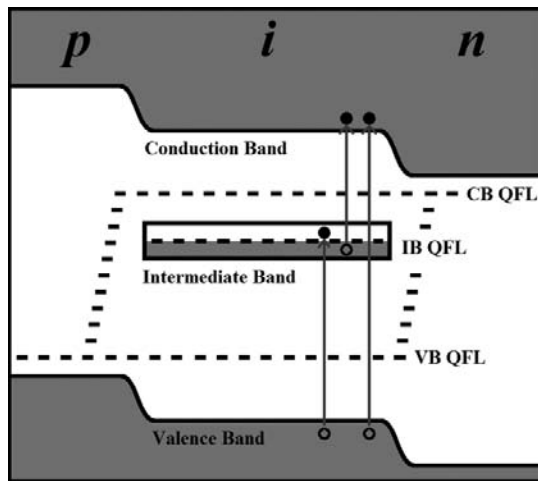


Figure 1: Ideal band diagram of the IBSC, with three distinct quasi-Fermi-levels (QFLs). Adapted from Luque [1].

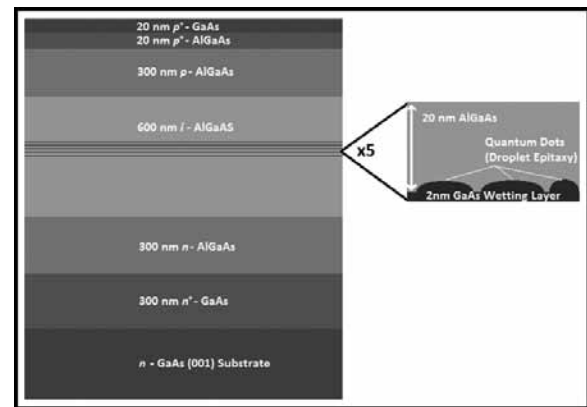


Figure 2: Fabricated QD-IBSC sample structure, grown by MBE.

Introduction and Motivation:

This research focused on studying the intermediate band solar cell (IBSC), which promises a great increase in photovoltaic conversion efficiency by extending the absorption range into the infrared while maintaining a high open circuit voltage. This is achieved by an intermediate band (IB) between the valence band (VB) and conduction band (CB), allowing the so called two-step photocurrent generation, wherein sub-bandgap photons produce a photocurrent by exciting the VB to IB, and IB to CB transitions in series (see Figure 1). The theoretical efficiency is 63% at maximum solar concentration, overcoming the Shockley-Queisser limit [1].

A widely used method of researching IBSCs employs embedded quantum dot (QD) layers. Many such efforts use lattice-mismatched materials because of the simplicity of dot formation. However, the resulting accumulated strain of many dot layers (which are necessary to absorb an appreciable amount of light) degrades the material quality, limiting the efficiency and masking intrinsic characteristics of the solar cell.

Here, we employed strain-free QDs fabricated in a lattice-matched system to eliminate strain related issues. To explore

the viability of such a material system for realizing an IBSC, we studied fundamental properties of GaAs/AlGaAs QD solar cells with a focus on the two-step photocurrent generation process, a fundamental operating principle of the IBSC.

Fabrication of Quantum Dot Solar Cells:

A QD solar cell device was grown on n-type gallium arsenide (GaAs) <100> substrate by molecular beam epitaxy (MBE). As illustrated in Figure 2, the device was an aluminum gallium arsenide (AlGaAs) p-i-n structure with five layers of quantum dots embedded within the *i* layer. Each QD layer was separated by a 20 nm thick AlGaAs buffer layer, so adjacent electronic states were decoupled. The GaAs QDs (Figure 3) were fabricated by using droplet epitaxy, wherein metallic Ga droplets were formed on a GaAs wetting layer by supplying Ga in an As-depleted environment, and then As was supplied to crystallize the Ga droplets into GaAs QDs.

In contrast to widely used InAs/GaAs QDs grown by the Stranski-Krastanov growth, these QDs were strain-free (GaAs

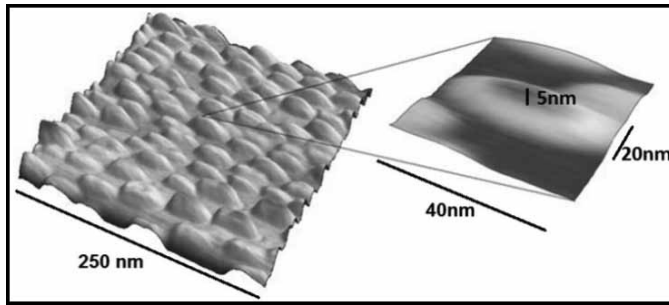


Figure 3: Visualization of QDs (inset to scale).

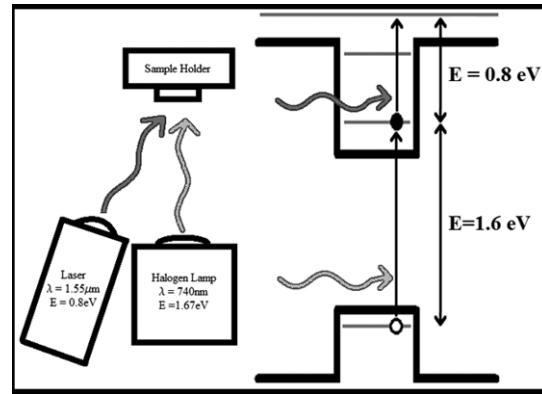


Figure 4: Experimental setup for two-step photocurrent measurements using 740 nm Halogen light.

and AlGaAs have nearly identical lattice constants), and the two-dimensional GaAs quantum well (QW) layer embedded underneath the QDs was controllable during growth. Here, the 2 nm thick QW layer was introduced to increase the confinement energy, aiming for suppression of thermal escape of carriers from the QDs and improved homogeneity of the QDs. The QW layer was doped n-type with Si, and the supplied electrons relax into the QDs.

Device Characterization:

As determined by atomic force microscopy (AFM), the resulting QD heights were 4.8 ± 0.8 nm, and each layer had an area density of 6.7×10^{10} /cm². Photoluminescence measurements at 20 K revealed nanostructure transitions with peaks at 1.6 eV and 1.67 eV, corresponding to the QDs and the wetting layer. This indicated that the barrier heights for electrons and holes are on the order of 100 meV, which is sufficiently high (compared to thermal energy, 26 meV, at room temperature) to limit thermal escape.

Photocurrent measurements at room temperature (using a Halogen lamp and a monochromator) demonstrated the absorption of photons with energies below the bandgap (1.8 eV) of AlGaAs. A reduction in photocurrent was observed, starting from negative bias and strengthening at higher biases (up to the open-circuit voltage). These current-voltage characteristics depended on the wavelength (λ) of light, and were explained in terms of the wavelength dependence of the absorption coefficient and the bias dependence of trapping efficiencies of electrons and holes by QDs.

To observe two-step absorption of sub-bandgap photons, we used the Halogen lamp and a 1.55 μ m (0.8 eV) laser (see Figure 4). The λ of the Halogen lamp was set at 740 nm (1.68 eV), generating carriers only in the QDs. Upon illumination of the sample with the laser, we observed an increase in photocurrent (ΔI), i.e., two-step photocurrent generation, and found that it depended largely on V . The increase in photocurrent was also

observed for shorter wavelengths (450 and 600 nm), where carriers were generated mostly in AlGaAs and then became trapped in the QDs. ΔI was at its maximum at -0.5-0.0 V, followed by a gradual reduction. This dependence of ΔI on V was qualitatively explained by the number of trapped carriers in QDs, and re-trapping of photoexcited carriers by the QDs.

Conclusions and Future Work:

We successfully fabricated lattice-matched GaAs/AlGaAs QD solar cells with five QD layers. A 2 nm thick GaAs wetting layer was embedded underneath each QD layer to suppress thermal escape of carriers generated in the QDs. Current-voltage characteristics were analyzed by comparison to the bias dependence of carrier trapping and absorption coefficients. We observed two-step photocurrent generation due to absorption of sub-bandgap photons, which is necessary for the operation of IBSCs. These results demonstrate the potential of GaAs/AlGaAs QD SCs.

Future work is needed to fully understand the dependences of the two-step process on voltage and incident energy, and will focus on identifying and tuning the necessary parameters to optimize the IB to CB transition.

Acknowledgements:

I would like thank Drs. Noda, Elborg, and Sakaki for their help, patience, and useful discussions; and the National Science Foundation and the National Nanotechnology Infrastructure Network International Research Experience for Undergraduates Program for funding this opportunity.

References:

- [1] A. Luque, et al. Nature Photonics 6, 146-152 (2012).

Spin Manipulation of Antiferromagnetic Devices

Alice Perrin

Physics, The College of William and Mary

NNIN REU Site: Cornell NanoScale Science and Technology Facility, Cornell University, Ithaca, NY

NNIN REU Principal Investigator: Dr. Daniel Ralph, Physics, Cornell University

NNIN REU Mentor: Gregory Stiehl, Physics, Cornell University

Contact: aeperrin@email.wm.edu, dcr14@cornell.edu, gms263@cornell.edu

Abstract:

Antiferromagnets (AF), the most common type of magnetically ordered material, exhibit a zero net magnetic moment below a specific temperature, called the Néel temperature, which renders them unresponsive to manipulation by magnetic fields [1]. Previous works have manipulated AF moments indirectly by way of the exchange spring effect, where a magnetic field is used to manipulate a ferromagnet exchange coupled to an AF [2]. Our recent work focused on reproducing this method of AF manipulation through observing tunneling anisotropic magnetoresistance (TAMR) in antiferromagnetic devices in which the antiferromagnet is interfaced with a tunnel junction. The TAMR effect is a change in the resistance through the AF/tunnel junction barrier due to the rotation of the AF moments. Our finished devices exhibited TAMR, thus demonstrating the successful manipulation of the AF magnetic moments through exchange coupling. Future work will introduce magnetocrystalline strain on the devices as another means with which to manipulate the moments.

Introduction:

A better understanding of the dynamics of AF magnetic moments could lead to antiferromagnetic components in magnetic memory storage and a broader range of materials available for use in electronics [1]. Antiferromagnets used as spin torque driven resonators would also allow for further study in the terahertz frequency range. However, because antiferromagnets cannot be manipulated by magnetic fields, other methods must

be explored in order to study them. One means of manipulating the AF moments is to interface the antiferromagnet with a ferromagnet. Below the blocking temperature there is an exchange coupling effect, and each AF moment is pinned to a corresponding ferromagnetic moment. In a magnetic field, the AF moments resist the rotation of the ferromagnetic moments until it becomes energetically advantageous for the coupled moments to rotate. However, the AF moments rotate non-uniformly, experiencing a winding effect, seen in Figure 1.

We observed the tunneling anisotropic magnetoresistance effect (TAMR) in order to confirm the success of the exchange coupling. TAMR is an effect in which we see a change in the resistance of a device comprising a tunnel junction interfaced with an antiferromagnet, where the antiferromagnet acts as a single magnetic electrode [3]. This change in resistance occurs because the density of states at the interface changes as the AF moments rotate. As the density of states decreases, less electrons will be able to tunnel through the junction, and there will therefore be a higher resistance through the device.

Fabrication:

We began fabrication of our devices by sputtering a stack of materials onto a 200 micron silicon wafer in a magnetic field. From the substrate upward, the stack was made up of: Ta(5)/Ru(10)/Ta(5)/NiFe(0-10)/IrMn(3)/MgO(2-3)/Ta(3)/Ru(10) where the number after each layer is its thickness in nanometers.

The bottom layers of Ta/Ru/Ta made up the bottom electrode of our devices. The next layers contained a NiFe ferromagnetic layer, antiferromagnetic IrMn, a MgO tunnel junction, and a top electrode of Ta/Ru. The finished devices allowed us to pass a current through a pillar containing the ferromagnet, antiferromagnet, and tunnel junction in order to measure the resistance of the stack. These

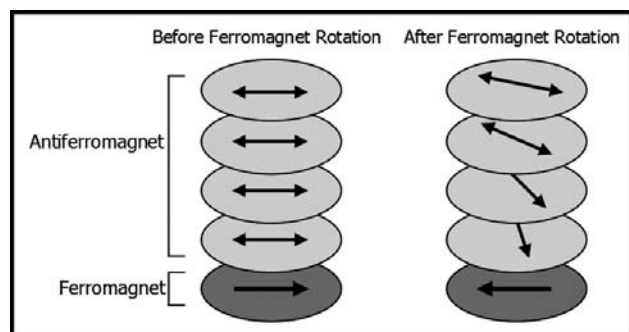


Figure 1: When exchange-coupled, the rotation of the antiferromagnetic moments is non-uniform.

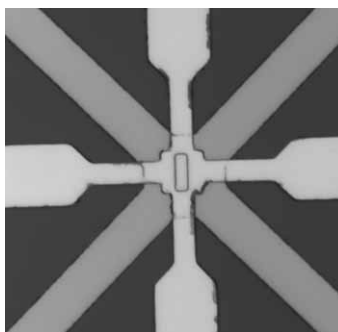


Figure 2: A top view of a finished device with a 3 by 9 μm pillar.

pillars ranged in surface area (as seen from the top) from $1 \times \frac{1}{2} \mu\text{m}$ to $10 \times 5 \mu\text{m}$ to allow us to examine the role of the area on the TAMR effect.

Results and Conclusions:

We gathered data from devices with layers NiFe(10)/IrMn(3)/MgO(2.5) nm, cooling them to temperatures ranging from 2.2K to 50K. We measured the resistance of the devices versus the magnetic field, which swept over a range large enough to induce moment rotation in the coupled ferromagnet and antiferromagnet. In Figure 3, we can see two clear steady resistance states where the slope of the data is near zero. The device switched between these states at ± 500 Oe depending on whether the field was sweeping negatively or positively, due to the drag caused by the antiferromagnet moments resisting rotation. This, along with the two resistance states, provides qualitative evidence of TAMR in our devices and therefore demonstrates successful manipulation of the AF moments through exchange coupling.

Future Work:

Future work on this project will incorporate the use of strain as an addition means of manipulating the AF moments by altering the magnetocrystalline anisotropy of the antiferromagnet. This will redefine the rotation angles at which the energy of the moments are at a minima, allowing for a method of manipulating the moments directly. Our method of inducing strain on the devices can be seen in Figure 4. Strain will be explored as both a supplement to and a replacement for exchange coupling as a means to manipulate the AF moments.

Acknowledgments:

Thank you to the National Science Foundation, National Nanotechnology Infrastructure Network Research Experience for Undergraduates Program, Cornell NanoScale Facility, and Cornell Center of Materials Research for providing all the

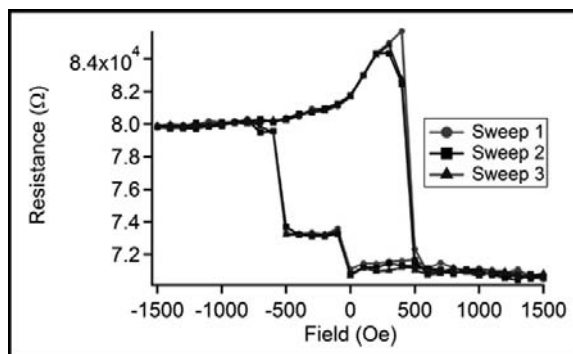


Figure 3: A hysteresis curve demonstrating stable resistance states around 70 kΩ and 80 kΩ, indicative that AF moment rotation has occurred.

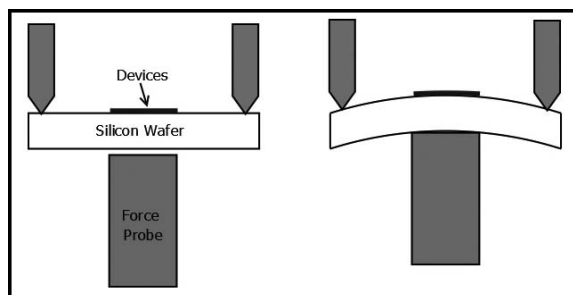


Figure 4: The wafers can be laterally manipulated by a three point strain induction system.

funds and facilities for this project. A special thanks to Dan Ralph, Greg Stiehl, the Ralph group, the CNF Staff, and Rob Ilic and Melanie-Claire Mallison.

References:

- [1] Shick, A.B., et al.; "Spin-orbit Coupling Induced Anisotropy Effects in Bimetallic Antiferromagnets: A Route Towards Antiferromagnetic Spintronics"; Physical Review B, 81, 1-4 (2010).
- [2] Marti, X.; "Electrical Measurements of Antiferromagnetic Moments in Exchange-Coupled IrMn/NiFe Stacks"; Phys.Rev.Let., 108, 1-4 (2012).
- [3] Park, B.G., et al.; "A Spin-valve-like Magnetoresistance of an Antiferromagnet-based Tunnel Junction"; Nature Mats, 10, 347-51, 2011.

Nano-Structuring Diamond for Quantum Sensing

Kevin Tkacz

Physics, Carnegie Mellon University

NNIN REU Site: UCSB Nanofabrication Facility, University of California, Santa Barbara, CA

NNIN REU Principal Investigator: Prof. Ania Bleszynski Jayich, Physics, University of California, Santa Barbara

NNIN REU Mentor: Preeti Ovarthaiyapong, Physics, University of California, Santa Barbara

Contact: ktkacz@andrew.cmu.edu, ania@physics.ucsb.edu, pov@physics.ucsb.edu

Abstract and Introduction:

The ability to structure diamond on the nanoscale is crucial for realizing diamond's potential as nano electro-mechanical material. In particular diamond plays host to the nitrogen-vacancy center, an atom-like defect that is promising for quantum sensing applications. Processing of diamond, however, is difficult and not well established as diamond is the hardest known material and is chemically inert.

In this work, we have pursued two techniques to achieve efficient and controlled diamond structuring. First, we used chemical mechanical polishing (CMP) to planarize and smooth diamond samples. Using 6 μm diameter diamond powder in an ethane-diol suspension, polishing rates were less than 10 μm per hour. Scratching of the diamond surface by the nanodiamond powder was observed. Second, we explored an Ar/CF₄/O₂ inductively coupled plasma (ICP) etch and found the diamond etch rate to be 16.7 μm per hour. The surface quality depends heavily on the smoothness of the starting surface, with any irregularities in the starting surface becoming more pronounced after etching. Achieving a fast and smooth diamond thinning process will enable the production of high-quality diamond nanostructures for enhanced sensing.

Experimental Procedure:

The CMP functions similarly to sandpaper. A sample surface is brought into contact with a rotating polishing pad with slurry applied between them. The surface is polished as it contacts the pad through the slurry. We used a 6 μm diameter diamond powder in ethane-diol polishing fluid as our slurry. The samples we worked with were 2 mm by 2 mm, and therefore needed an increase in back pressure while polishing to make adequate contact with the polishing pad. The increased back pressure made the sample carrier convex, which pushed the small sample downward into the pad. Parameters which were considered when using the CMP were the table speed and carrier speed (the speeds of rotation of each body), slurry type and flow rate, and down force or the amount of force applied when pushing the sample into the pad.

The ICP etcher bombards a sample in a vacuum chamber with reactive plasma ions to etch through the bombarded surface. There are many parameters to manipulate when using the ICP including the ICP power, bias power, vacuum pressure, gas composition, and gas flow rate. We used an ICP power of 1000 W, vacuum pressure of 2 Pa and a gas composed of O₂, Ar, and CF₄. Before and after etching, scanning electron microscopy (SEM) was used to examine the quality of the surface, and step profilometry was used to determine etch depths from which etch rates were extracted. Etches were performed on two types of diamond surfaces, which varied in initial quality.

Results and Conclusions:

The polishing rate of diamond is very slow. It has been determined to be less than 10 μms per hour based on the resolution of our height measurements and could be considerable slower than this. The change between Figure 1, the diamond surface before polishing, and Figure 2, the diamond surface after polishing for 40 minutes, is minimal. It remains to be seen whether this process is simply slow and additional polishing time would help or if significant modification to the polishing technique is needed.

We have achieved etching that is both fast and yields areas of minimal pitting as seen in Figure 3. This etch was achieved at a rate of 16.7 μm per hour which is much faster than other etches that yield such quality surfaces. While this etch did yield areas of the sample that had minimal pitting, there are areas that had much more severe deformations. This is likely due to surface defects prior to etching, but should be investigated further.

One very clear result was that the starting diamond surface is important. A smooth starting surface will yield smoother results while a rougher starting surface will become more pitted and its defects will become more pronounced through etching. This is evident when comparing Figure 3 to Figure 4, which shows the same etch on a rougher starting surface.

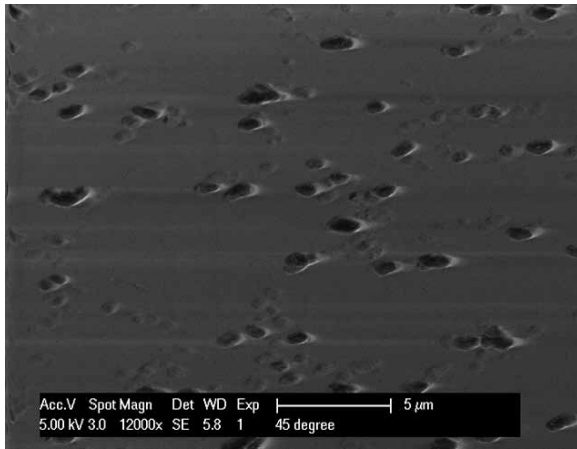


Figure 1: SEM image of diamond surface before polishing.

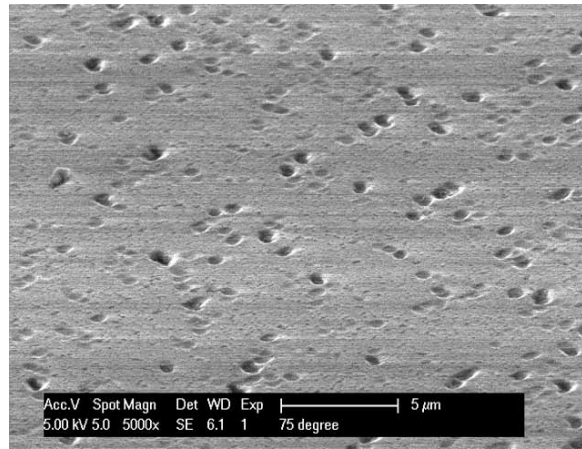


Figure 2: SEM of diamond surface after polishing for 40 min.

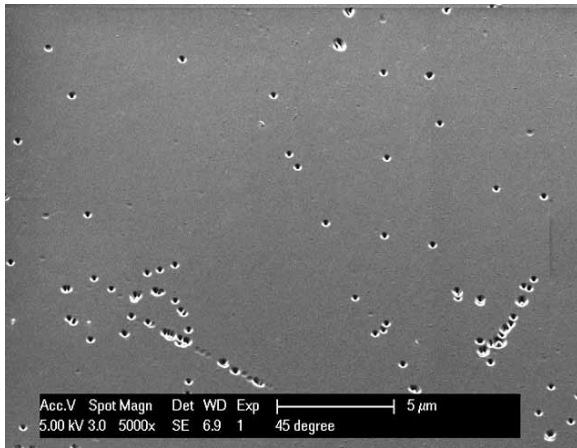


Figure 3: SEM image of etched surface with minor pitting.

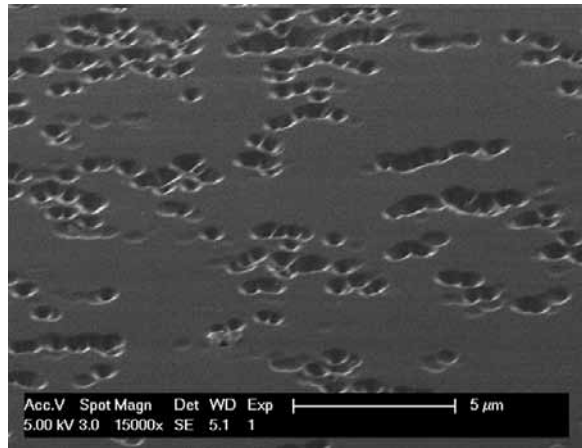


Figure 4: SEM image of etched surface with a great deal of pitting.

We also repeated this same etch on the same type of surface, but reduced the bias to one half of the original value. This etch was significantly slower (closer to 3 μm per hour) and resulted in a highly pitted surface.

Future Work:

More precise determination of the diamond polish rate is required. While we have achieved a useful etch, the parameter space is not entirely understood. Further investigation into this is needed to optimize the etching process. Making adjustments to the bias power or the ICP power should be the first variables to be considered when exploring this parameter space further.

Finally, the effects of these modeling techniques on nitrogen-vacancy centers need to be investigated.

Acknowledgments:

I would like to thank Preeti Ovarthaiyapong, Professor Ania Bleszynski Jayich, and the Jayich group for their help this summer. I would also like to thank the University of California, Santa Barbara clean room engineers who helped me along the way and my fellow University of California, Santa Barbara National Nanotechnology Infrastructure Network interns who made my summer truly enjoyable. I would also like to thank the National Nanotechnology Infrastructure Network Research Experience for Undergraduates Program, the Air Force Office of Scientific Research, the University of California, Santa Barbara, and the National Science Foundation for funding me and providing me with the resources to work this summer.